A Comparative Study of Synchronous Current Control Schemes Based on FCS-MPC and PI-PWM for a Two-Motor Three-Phase Drive

Chee Shen Lim, *Student Member*, *IEEE*, Emil Levi, *Fellow*, *IEEE*, Martin Jones, Nasrudin Abd. Rahim, *Senior Member*, *IEEE*, Wooi Ping Hew, *Member*, *IEEE*

***Abstract* – A two-motor drive, supplied by a five-leg inverter, is considered in the paper. The independent control of machines with full dc-bus voltage utilization is typically achieved using an existing pulse width modulation (PWM) technique in conjunction with field-oriented control, based on PI current control. However, model predictive control (MPC), based on a finite number of control inputs (finite-control-set MPC, FCS-MPC) does not utilize a pulse width modulator. The paper introduces three FCS-MPC schemes for synchronous current control in this drive system. The first scheme uses all the available switching states. The second and the third scheme are aimed at reducing the computational burden and utilize a reduced set of voltage vectors and duty ratio partitioning principle, respectively. Steady-state and transient performance are analyzed and compared both against each other, and with respect to the field-oriented control based on PI controllers and PWM. All analyses are experimental and use the same experimental rig and test conditions. Comparison of the predictive schemes leads to the conclusion that the first two schemes have the fastest transient response. The third scheme has a much smaller current ripple, while achieving perfect control decoupling between the machines, and is of low computational complexity. Nevertheless, at approximately the same switching loss, the PI-PWM control yields the lowest current ripple but with slower electrical transient response.**

I. Introduction

Multi-motor three-phase drives with reduced-switch-count supply have been studied in the past using various voltage source inverter (VSI) topologies. A two-motor three-phase drive can be supplied by a five-leg VSI [1].

Model predictive control (MPC) has been widely studied in conjunction with drives during the last decade and the most frequent form is the FCS-MPC. Various control schemes based on FCS-MPC, including current [2], flux and torque [3,4], speed [5], and sensorless speed [6] control, have been reported. Despite its generality, one practical problem is associated with the computational burden, which in turn depends on the number of inverter switching states. In the reduced-switch-count multi-motor drive topology studied here, an m-motor drive requires $(2m+1)$ inverter legs. For a two-level inverter, a total of 2^{2m+1} switching states are available. While a two-motor drive has only 32 switching states, a four-motor drive will have 512 switching states. In essence, the computational burden of the FCS-MPC increases exponentially with the number of machines.

Integration of the FCS-MPC into drives has led to the development of techniques with a reduced computational burden, at the expense of control optimality. For example, adjacent vector principle in multi-level inverters [7], restrained search technique in multiphase drives [8], and use of only adjacent switching states in multi-motor drives with reduced-switch-count inverter [9] have been reported. Nevertheless, an evaluation of the control quality using full and reduced sets of switching states has never been detailed. The only work with a somewhat similar idea is [10], where a drive system with 32 VSI output voltage states has also been considered. However, the work in [10] is related to a single five-phase induction motor drive, supplied from a five-phase VSI and the switching state number is reduced by considering voltage vector magnitudes (small, medium and large inverter voltage vectors, which come in the sets of 10, plus two zero vector states). This is completely different from the situation elaborated here, where there are two three-phase machines supplied using an inverter with five-legs (which imposes a constraint on the available output voltage vectors) and where all vectors are of the same magnitude, so that different principles of the switching state set reduction have to be used. Further, the system considered here requires two predictive models since there are two machines, and therefore the cost function used has to be associated with the both motors.

The paper has two main objectives. The first one is development, evaluation and comparison of the computational complexity and performance of three FCS-MPC schemes applied to a two-machine three-phase induction motor drive. The second one is the comparison with the rotor flux-oriented control based on PI controllers and PWM (known as PI-PWM control), using PWM of [1, 11]. All the considered schemes utilize synchronous current control for both motors. The first scheme, MPC1, includes all the available switching states of the five-leg inverter in the optimization algorithm. The second scheme (MPC2) uses the adjacent voltage vector principle for algorithm simplification. Similar method has been used in [9], but no detailed analysis of the impact of the simplification on overall performance was given. The third scheme (MPC3) is based on the duty ratio partitioning principle, which in essence decouples the optimization process between the two motors, and leads to low computational burden. It is meant

Manuscript received March 14, 2013; revised July 01, 2013 and August 13, 2013. Accepted September 15, 2013.

C.S. Lim is with the University of Malaya, UMPEDAC Research Center, Kuala Lumpur, Malaysia and was, during the research described here, also with the Liverpool John Moores University, School of Engineering, Technology and Maritime Operations, Liverpool L3 3AF, U.K. (e-mail: limcheeshen@gmail.com).

E. Levi and M. Jones are with the School of Engineering, Technology and Maritime Operations, Liverpool John Moores University, Liverpool L3 3AF, U.K. (e-mails: e.levi@ljmu.ac.uk and m.jones2@ljmu.ac.uk).

N.A. Rahim and W.P. Hew are with the UMPEDAC Research Centre, Wisma R&D, University of Malaya, 59990, Kuala Lumpur, Malaysia (e-mails: nasrudin@um.edu.my and wphew@um.edu.my).

to solve the issue of exponentially increasing computational complexity of the FCS-MPC in this multi-motor drive configuration.

The rest of the paper is organized as follows. Section II introduces the two-motor drive topology and derives the predictive model of the three-phase induction motors and the five-leg inverter for the machine's state prediction in the MPC algorithms. Section III describes MPC1, MPC2, MPC3, and PI-PWM control schemes. Section IV analyses the steady-state performance in terms of average current ripple and average switching frequency. Section V compares the transient performance of all the considered current control schemes. Section VI summarizes the results of the comparison, while Section VII concludes the paper.

II. The Two-Motor Three-Phase Drive System and the Dicretised Model

Fig. 1 shows a general configuration of a two-motor three-phase drive supplied by a five-leg VSI. Phase-*c* of each machine is connected to the leg-*C* of the inverter. The dc-bus voltage is typically set to the value corresponding to a single-motor drive's need. This results in voltage constraint on the drive system, which subsequently limits the operating speed ranges of the two motors. Higher current flow in the shared inverter leg is also a known problem. Both limitations have been discussed in detail in [1, 11] and remain to be present in this work as well.

In general, a generic model predictive control algorithm has two stages: model prediction stage and cost minimization stage [2]. In the two-motor three-phase drive, a five-leg inverter has 32 switching states. A complete evaluation of this control input set would require 32 sets of variable predictions and cost computations for optimization. However, due to the presence of redundancy in this drive configuration, the control algorithm needs to predict the future machine states for only seven effective voltage vectors per motor, in the model prediction stage [9]. Nevertheless, the cost minimization stage still requires evaluation of all 32 switching states. In what follows, the predictive model, used by all the MPC schemes, is illustrated on per-machine basis. Next, a general cost function, realizing simultaneous tracking of the two motors' synchronous current components, is given. Details of the cost minimization and other properties of MPC1, MPC2 and MPC3 are explained in Section III.

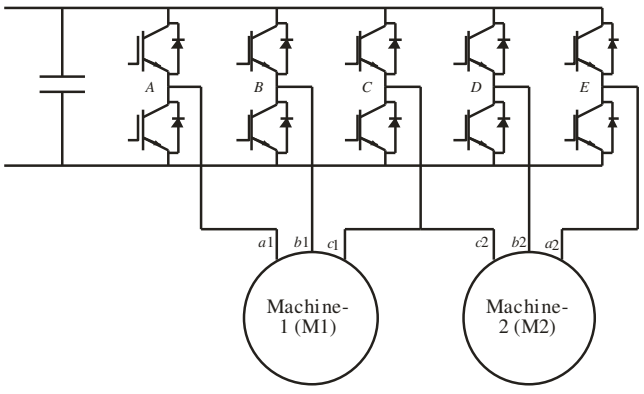

Fig. 1. Electrical connections of the two three-phase motors and the five-leg VSI.

A. Predictive Model

The continuous-time state-space model of a three-phase induction machine with stator current and rotor flux components chosen as the state-space variables is given with

$$\dot{\mathbf{x}}(t) = \mathbf{A}_t \mathbf{x}(t) + \mathbf{B}_t \mathbf{u}(t) \tag{1}$$

where

$$\mathbf{x} = \begin{bmatrix} i_{sd} & i_{sq} & \psi_{rd} & \psi_{rq} \end{bmatrix}^T, \ \mathbf{u} = \begin{bmatrix} v_{sd} & v_{sq} \end{bmatrix}^T.$$

$$\mathbf{A}_t = \begin{bmatrix} -(\frac{1}{\sigma T_s} + \frac{1-\sigma}{\sigma T_r}) & \omega_{rf} & \frac{1-\sigma}{\sigma L_m T_r} & \frac{\omega_{re}(1-\sigma)}{\sigma L_m} \\ -\omega_{rf} & -(\frac{1}{\sigma T_s} + \frac{1-\sigma}{\sigma T_r}) & -\frac{\omega_{re}(1-\sigma)}{\sigma L_m} & \frac{1-\sigma}{\sigma L_m T_r} \\ \frac{L_m}{T_r} & 0 & -\frac{1}{T_r} & \omega_{sl} \\ 0 & \frac{L_m}{T_r} & -\omega_{sl} & -\frac{1}{T_r} \end{bmatrix},$$

$$\mathbf{B}_t = \begin{bmatrix} \frac{1}{\sigma L_s} & 0 \\ 0 & \frac{1}{\sigma L_s} \\ 0 & 0 \\ 0 & 0 \end{bmatrix}$$

T_s and T_r are the stator and rotor time constants, L_m is the mutual inductance, σ is the total leakage coefficient, ω_{re}, ω_{sl}, and ω_{rf} are the rotor electrical speed, the slip speed, and the rotor flux speed. Note that the state matrix $\mathbf{A}_t$ is time-varying, due to the speed terms, while the input matrix $\mathbf{B}_t$ is not. Model (1) can be written in discrete-time form as

$$\mathbf{x}(k+1) = \mathbf{F}_k \mathbf{x}(k) + \mathbf{G}_k \mathbf{u}(k) \tag{2}$$

where, using forward-Euler discretization method, $\mathbf{F}_k = (1+\mathbf{A}_t T)$ and $\mathbf{G}_k = \mathbf{B}_t T$ at time $t=kT$. ω_{sl} and ω_{rf} are obtained using the feed-forward principle [12]:

$$\omega_{sl} = \frac{R_r i_{sq}^*}{L_r i_{sd}^*} \tag{3}$$

$$\omega_{rf} = \omega_{re} + \omega_{sl} \tag{4}$$

It has been verified in [10, 12] that, since (3) includes the assumption of zero *q*-axis rotor flux component and current control is fast, there is no need to estimate the *q*-axis rotor flux component. The conclusion follows intuitively from the principles of the rotor flux oriented control, where in the reference frame determined by the indirect rotor flux oriented controller the *q*-axis component of the rotor flux is by default zero (regardless of the true value in the machine, which may differ due to parameter variation effects). Nevertheless, during the course of the investigation it has been confirmed by simulation that the inclusion of the *q*-axis rotor flux estimation in the predictive model gives values negligibly different from zero, so that there is no impact on the control performance (but the predictive model is more complicated). This greatly simplifies the predictive model, especially here where there are two machine models. The discrete-time machine model is simplified to the form of (2) with the following coefficients and variables:

$$\mathbf{x} = \begin{bmatrix} i_{sd} & i_{sq} & \psi_{rd} \end{bmatrix}^T, \ \mathbf{u} = \begin{bmatrix} v_{sd} & v_{sq} \end{bmatrix}^T, \tag{5}$$

$$\mathbf{F}_k = \begin{bmatrix} 1 - T(\frac{1}{\sigma T_s} + \frac{1-\sigma}{\sigma T_r}) & T\omega_{rf,k} & \frac{T(1-\sigma)}{\sigma L_m T_r} \\ -T\omega_{rf,k} & 1 - T(\frac{1}{\sigma T_s} + \frac{1-\sigma}{\sigma T_r}) & -\frac{T\omega_{re,k}(1-\sigma)}{\sigma L_m} \\ \frac{TL_m}{T_r} & 0 & 1 - \frac{T}{T_r} \end{bmatrix}$$

$$\mathbf{G}_k = \begin{bmatrix} \frac{T}{\sigma L_s} & 0 \\ 0 & \frac{T}{\sigma L_s} \\ 0 & 0 \end{bmatrix}$$

The standard two-step-ahead prediction is used to overcome the high computational delay. The first-step stator current components $i_{sd}(k+1)$ and $i_{sq}(k+1)$, and the d-axis rotor flux component $\psi_{rd}(k+1)$ are estimated using (2). $v_{sd}(k)$ and $v_{sq}(k)$ correspond to the synchronous stator d- and q-axis voltages being realized from instant k to $(k+1)$. Then, the second-step stator current components $i_{sd}(k+2)$ and $i_{sq}(k+2)$, which are required in the cost function, are predicted, based on (2) from instant $(k+1)$ to $(k+2)$, using the first-step predicted variables and the inverter voltages at instant $(k+1)$ expressed in the synchronous reference frame:

$$\begin{bmatrix} v_{sd}(k+1) \\ v_{sq}(k+1) \end{bmatrix} = \mathbf{R}_{k+1}\mathbf{C}\frac{V_{dc}}{3}\begin{bmatrix} 2 & -1 & -1 \\ -1 & 2 & -1 \\ -1 & -1 & 2 \end{bmatrix}\mathbf{S}(k+1) \quad (6)$$

$$\mathbf{C} = \frac{2}{3}\begin{bmatrix} 1 & \cos(2\pi/3) & \cos(4\pi/3) \\ 0 & \sin(2\pi/3) & \sin(4\pi/3) \end{bmatrix} \quad (7)$$

$$\mathbf{R}_{k+1} = \begin{bmatrix} \cos\theta_{rf,k+1} & \sin\theta_{rf,k+1} \\ -\sin\theta_{rf,k+1} & \cos\theta_{rf,k+1} \end{bmatrix} \quad (8)$$

$$\theta_{rf,k} = \theta_{re,k} + \theta_{sl,k-1} + \frac{T}{2}(\omega_{sl,k-1} + \omega_{sl,k}) \quad (9a)$$

$$\theta_{rf,k+1} = \theta_{rf,k} + T(\omega_{re,k} + \omega_{sl,k}) \quad (9b)$$

Here V_{dc} is the dc-bus voltage, $\mathbf{C}$ is the standard decoupling transformation, $\mathbf{R}_{k+1}$ is the standard rotational transformation that uses the projected rotor flux angle at instant $(k+1)$, i.e. $\theta_{rf,k+1}$, calculated using (9b). Further, $\mathbf{S}=[s_a\ s_b\ s_c]^T$, where $s_i=\{0,1\}$ and $i = a$, b, and c, indicates the three-phase switching state of the three inverter legs where the machine phases a, b, and c are connected. Machine-1 and Machine-2 are connected to inverter legs A, B, and C, and legs E, D, and C, respectively.

The estimation of the rotor flux component is based on an open-loop observer without any corrective feedbacks (in contrast to stator current predictions). While deviation has been proven to exist in the estimated rotor flux vector of a stationary-axis based machine model, it is established from numerical simulations that no deviation is present in this first-order discretized synchronous-axis based machine model. This is so since the rotor flux vector in the stationary reference frame is ac in nature (while it is dc in the synchronous reference frame) and hence estimating it using a low-order discretisation technique without any corrective feedback is not sufficient. This becomes obvious especially when the sampling frequency of MPC is relatively low.

B. Cost Function

Tracking of the flux and torque producing currents for each individual machine can be realized using cost components j_{M1} and j_{M2}:

$$j_{M1} = [i^*_{sd1}(k+2) - i_{sd1}(k+2)]^2 + [i^*_{sq1}(k+2) - i_{sq1}(k+2)]^2 \quad (10)$$

$$j_{M2} = [i^*_{sd2}(k+2) - i_{sd2}(k+2)]^2 + [i^*_{sq2}(k+2) - i_{sq2}(k+2)]^2 \quad (11)$$

where $i^*_{sd1}(k+2)$, $i^*_{sq1}(k+2)$, $i^*_{sd2}(k+2)$ and $i^*_{sq2}(k+2)$ are, respectively, the projected future current references at horizon $(k+2)$, which have been assumed to be the same as the current references at $t=kT$. This is due simply to the fact that future flux and torque requirements are not available in typical drive operation. Eventually, the simultaneous operation of the two machines is achieved using a general cost function J:

$$J = j_{M1} + \lambda_i j_{M2} \quad (12)$$

where $\lambda_i = (i_{sn1}/i_{sn2})^2$ is the normalization factor of the current errors with i_{sn1} and i_{sn2} being the rated currents of the two machines, respectively. In this study, since machines with the same rating are used, λ_i is 1. The shared-leg topology is considered using the algorithm given in the Appendix.

III. FCS-MPC And PI-PWM Control Schemes

Operating principles of MPC1, MPC2, and MPC3 are explained first and their computational complexity and maximum switching frequencies are then discussed. Next, the PI-PWM control is described. For all schemes, the same PI speed controller is used for closed-loop speed control.

A. MPC1

All switching states of the five-leg inverter are considered by this scheme. In Section II, the future stator currents are predicted on the per-machine basis using basically the three-phase switching states from {000} to {111}. In the cost minimization stage, algorithm (18) of the Appendix is used to evaluate only those combinations of the two sets of three-phase switching state sets **S** in (6) (further referred to as **S**1 for Machine-1 and **S**2 for Machine-2) that have the same switching state for the inverter leg-C, while eliminating combinations with different phase-c/leg-C state (the hard constraint imposed by the shared-leg structure).

It should be noted that whenever a five-leg zero switching state is chosen during the optimization stage, the switching state (either {00000} or {11111}) that gives the lowest number of commutations will be realized. The control block diagram of the MPC1 is shown in Fig. 2.

B. MPC2

The main objective of MPC2 is to reduce the computational burden by reducing the number of voltage vectors considered by the algorithm, in every sampling period, to those neighboring the present one (on the per-machine basis). It has been shown in [9] that restricting the future voltage vectors to those having only one state change

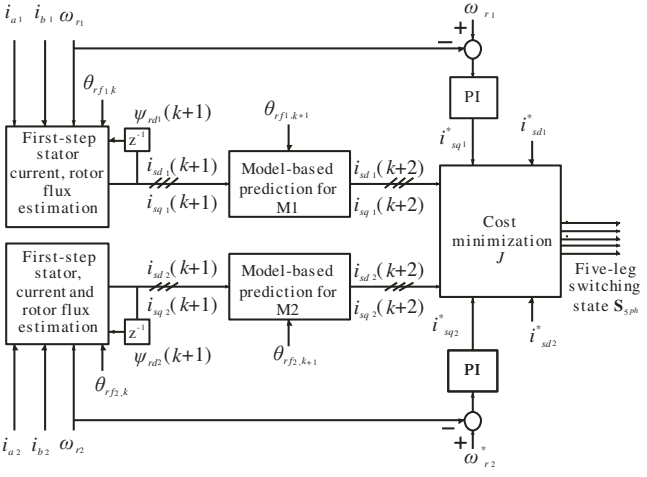

Fig. 2. Control block diagram for MPC1 and MPC2.

with respect to the present one, despite limiting the maximum switching frequency to only $0.2F_s$ (F_s is the algorithm sampling frequency) causes irregular disturbances in the synchronous current components. This is explained as the competition between the two machines in this shared-leg structure when only one zero switching state, the neighboring one, is included (per machine), although in principle a single-motor three-phase drive can operate properly with only one zero switching state. Thus, apart from those neighboring three-phase switching states (this already includes one zero switching state), the other zero switching state is taken into consideration in the MPC2. This however no longer limits the maximum switching frequency to $0.2F_s$.

Finally, MPC2 only evaluates the performance of switching combinations formed by **S**1 and **S**2 (five, instead of eight as in MPC1). Each **S** is comprised of switching states that form the present voltage vector, two neighboring active vectors, and the zero vector (with two states). The cost computation is realized using algorithm (18), and the algorithm computational complexity is shown in Table I.

C. MPC3 with Duty Ratio Partitioning

MPC1 inherently requires the common-leg structure to be considered during the cost function stage using algorithm (18); however, when higher number of machines (m) is considered, the cost computational burden increases along with the number of switching states (2^{2m+1}). The same applies also to MPC2, with slightly lower growing rate, despite the intended simplification using adjacent vector principle. Therefore, one of the objectives of MPC3 is to solve this shortcoming in multi-motor drives.

The shared-leg topology imposes a limit on the achievable quasi-sinusoidal voltage at inverter leg-C, requiring the two motors to operate within the given total voltage limit, as explained in [11]. Based on this property, a duty ratio principle is introduced into MPC3. It partitions each sampling period into two intervals, one per machine. During the first interval, the control algorithm chooses an appropriate voltage vector for Machine-1, and Machine-2 is subjected to a zero vector. Similar principle applies to the second interval in the opposite manner. A deterministic way to determine the duty ratio(s) is shown below.

The peaks of the fundamental voltages required by Machine-1 (V_{s1}) and Machine-2 (V_{s2}) are estimated using th steady-state stator voltage equilibrium equations:

$$\begin{aligned} V_{s1} &= \sqrt{[R_{s1}i_{sd1} - \omega_{rf1}\sigma_1 L_{s1}i_{sq1}]^2 + [R_{s1}i_{sq1} + \omega_{rf1}L_{s1}i_{sd1}]^2} \\ V_{s2} &= \sqrt{[R_{s2}i_{sd2} - \omega_{rf2}\sigma_2 L_{s2}i_{sq2}]^2 + [R_{s2}i_{sq2} + \omega_{rf2}L_{s2}i_{sd2}]^2} \end{aligned} \tag{13}$$

Assuming fast current tracking, the measured d- and q- axis currents in (13) can be replaced by the current references, to avoid appearance of "chattering" of switched currents in the estimated voltage values. At time kT, the peak voltages required during the instants (k+1) to (k+2) (see Fig. 3) are estimated using:

$$\begin{aligned} V_{s1,k+1} &= \sqrt{[R_{s1}i^*_{sd1}(k+2) - \omega_{rf1,k+1}\sigma_1 L_{s1}i^*_{sq1}(k+2)]^2 + [R_{s1}i^*_{sq1}(k+2) + \omega_{rf1,k+1}L_{s1}i^*_{sd1}(k+2)]^2} \\ V_{s2k+1} &= \sqrt{[R_{s2}i^*_{sd2}(k+2) - \omega_{rf2,k+1}\sigma_2 L_{s2}i^*_{sq2}(k+2)]^2 + [R_{s2}i^*_{sq2}(k+2) + \omega_{rf2,k+1}L_{s2}i^*_{sd2}(k+2)]^2} \end{aligned} \tag{14}$$

Note that $\omega_{rf,k+1}=\omega_{rf,k}$, owing to the assumed model time-invariant property within each optimization cycle. Based on the assumption of linear inverter operation, the used dc-bus voltage is approximated using $\sqrt{3}(V_{s1,k+1}+V_{s2,k+1})$. Then, duty ratios $d_{1,k+1}$ (for Machine-1) and $d_{2,k+1}$ (for Machine-2) between instants (k+1) and (k+2) are estimated using:

$$d_{1,k+1} = \begin{cases} \dfrac{\sqrt{3}V_{s1,k+1} + 0.5V_{s0,k+1}}{V_{dc}}, \text{where } \sqrt{3}(V_{s1,k+1} + V_{s2,k+1}) < V_{dc}, \text{and} \\ \qquad V_{s0,k+1} = V_{dc} - \sqrt{3}(V_{s1,k+1} + V_{s2,k+1}); \\ \dfrac{V_{s1,k+1}}{V_{s1,k+1} + V_{s2,k+1}}, \text{where } \sqrt{3}(V_{s1,k+1} + V_{s2,k+1}) \geq V_{dc}. \end{cases}$$

$$d_{2,k+1} = 1 - d_{1,k+1} \tag{15}$$

$V_{s0,k+1}$ corresponds to the excess dc voltage not used by the machines. This excess voltage is reserved for the control of stator d- and q-axis currents of the two motors during transient. For simplicity, $V_{s0,k+1}$ is allocated equally to each machine through the use of the 0.5 factor in (15). Ideally, $\sqrt{3}(V_{s1,k+1}+V_{s2,k+1})$ should not exceed V_{dc}. However, if this occurs in practice, e.g. due to parameter variation, the duty ratios are set proportionally using $V_{s1,k+1}$ and $V_{s2,k+1}$, given in (15). Moreover, it is noted here that the dead time is 4.8% (=3μs/62.5μs x 100%) of the sampling period. Therefore, a minimum value of 0.1 and maximum value of 0.9 are imposed on d_1 and d_2. This is to ensure that even with the presence of dead-time effect, and when e.g. M1 remains at standstill (i.e. very small V_{s1}) while M2 operates at high speed (i.e. very large V_{s2}), there is always a sufficient voltage allocated to M1 for the rated rotor flux operation.

The paragraph above explains how the duty ratios $d_{1,k+1}$ and $d_{2,k+1}$ are calculated. Fig. 3 illustrates the time intervals where $d_{1,k+1}$ and $d_{2,k+1}$ apply during the algorithm cycle at time kT, accounting for the two-step-ahead prediction. The voltage vector exerted on Machine-1 during $d_{1,k+1}T$ interval, i.e. due to **S**1(k+1), is selected through the optimization of j_{M1} in (10). The same applies to Machine-2 during $d_{2,k+1}T$ interval. Also, within $d_{1,k+1}T$ interval, the voltage vector exerted on Machine-2 is forced to zero by setting leg-D state (s_D) and leg-E state (s_E) the same as leg-C (s_C) (i.e. phase-c state of Machine-1). The same applies to Machine-1 within $d_{2,k+1}T$ interval. From Fig. 3, it is noted that whenever a zero switching state is chosen for Machine-1 during $d_{1,k+1}T$ interval, **S**1(k+1) can be either {000} or {111} since either of the zero five-leg switching states ({00000} or {11111}) can be selected, depending which one gives the lowest number of commutations in relation to the previous five-leg switching state (which was formed by **S**2(k)). For example, if **S**2(k) is {001}, which means that the corresponding five-leg switching state is {11100}, the zero voltage vector for Machine-1 in the $d_{1,k+1}T$ interval will be realized using {11111} instead of {00000}. The same applies to **S**2(k+1) but the consideration applies to the previous five-leg switching state formed by **S**1(k+1). The complete control block diagram of MPC3 is shown in Fig. 4.

D. Computational Complexity and Maximum Switching Frequency

Computational complexity of the considered FCS-MPC schemes is summarized in Table I. It can be seen that the number of variable predictions (P) increases linearly with the number of machines after eliminating the redundancy.

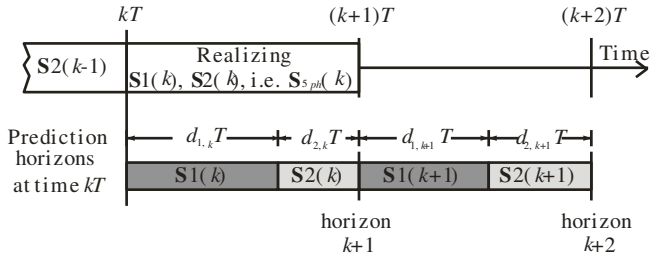

Fig. 3. Timing diagram for MPC3 illustrating the sequence of **S**1 and **S**2.

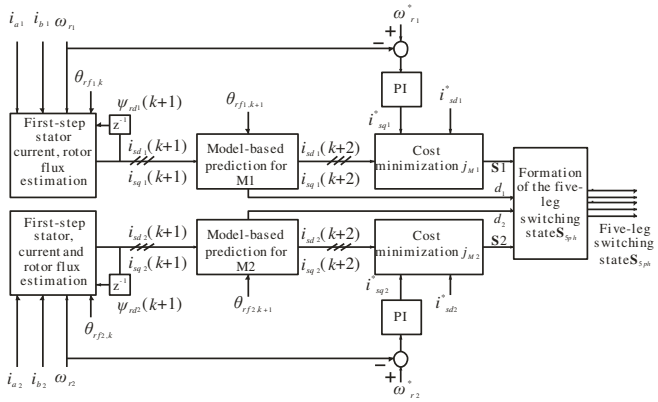

Fig. 4. Control block diagram for MPC3.

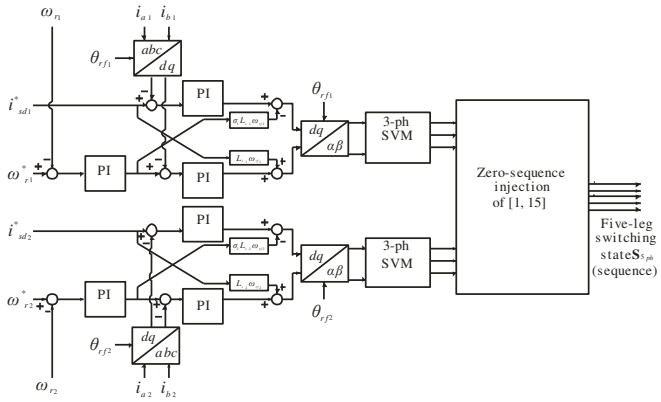

Fig. 5. Control block diagram for PI-PWM control.

TABLE I. COMPUTATIONAL COMPLEXITY OF FCS-MPC SCHEMES AND MAXIMUM SWITCHING FREQUENCY

Scheme	2-motor drive with 5-leg VSI		*m*-motor drive with (2*m*+1)-leg VSI		Max. switching freq. [Hz]
	P	Q	P	Q	
MPC1	14	31	7*m*	2^{2m+1}	$0.5F_s$
MPC2	8	13-17	4*m*	(3^m+2^m) to (4^m+1)	$0.4F_s$
MPC3	14	14	7*m*	7*m*	$0.8F_s$

Exponentially increasing number of cost computations (Q) is still present in MPC1 and MPC2 with respect to the number of machines, while MPC3 has only linearly-increasing cost computational complexity. This is so since (14)-(15) are only calculated once per optimization cycle, and hence incur only a small computational burden.

The maximum switching frequency is deduced from the maximum possible number of commutations that can be attained in the FCS-MPC schemes times $(1/2n)F_s$, where n is the number of inverter legs, n=2m+1. Maximum five commutations can be attained in MPC1, leading to a maximum switching frequency of $0.5F_s$. MPC2 can have a maximum of four commutations, given by e.g. changing from {000} to {111} for **S**1, while **S**2 can only have one state change (the change from {000} to {111} is not allowed, as this would eventually lead to the change from {00000} to {11111}; this is not permitted from the outset due to the minimum commutation consideration). On the other hand, MPC3 has only a maximum of eight commutations, rather than ten at the first sight. This is explained using Fig. 3. The three-phase switching state for Machine-1, **S**1(k+1), is always preceded by a zero state (either {000} or {111}) depending on **S**2(k) (Fig. 3); the same applies to **S**2(k+1), which is always preceded by zero state ({000} or {111}), depending on **S**1(k+1). Only a maximum of two commutations are possible when the three-phase switching state changes from a zero to an active vector (again, changing between the zero switching states is not permitted from the outset). This eventually leads to only a maximum of four commutations during the time instant $(k+1)T$ (e.g. two in legs-*A* to *C*, and two in legs-*D*, *E*), while another four is possible for the time instant $(k+d_{1,k+1})T$ (e.g. two in legs-*A*, *B*, and two in legs-*D*-to-*E*). Thus, it follows that MPC3 has a maximum switching frequency of $0.8F_s$.

E. PI-PWM Control

The realization of PI-PWM control is based on the standard two-motor field-oriented control scheme and a PWM technique with arbitrary dc-bus voltage allocation of [1, 11], which provides full dc-bus voltage utilization. The control is implemented in the rotor flux-oriented reference frame, using the rotor flux angle obtained by means of the indirect feed-forward method (9a). The complete PI-PWM control scheme is depicted in Fig. 5. For a fair comparison, the PI-PWM control scheme is complemented with the standard stator voltage decoupling terms in order to improve the dynamics. The PI current controller parameters are tuned in an empirical manner to give the best possible control performance, for the sake of fairness in the comparison. Outputs of the four PI controllers (two for each machine) are modulated using the PWM of [1, 11] to form the five-leg inverter switching states.

IV. STEADY-STATE PERFORMANCE COMPARISON

Although all the control algorithms have been first verified using numerical simulations, the following analyses are based entirely on the experimental results, since they give a better representation of the control performance in the presence of non-ideal properties, such as model uncertainty, measurement noise, inverter dead-time effects, etc.

Fig. 6 shows the experimental test rig. The load is inertial, of the same value for both motors. The feedback signals are provided by four phase current measurements (two per machine) and two resolvers. Due to the hardware restrictions, the dc-bus voltage is set to 450V. The FCS-MPC algorithm sampling frequency is 16kHz; the data sampling frequency is either 8kHz or 16kHz, depending on the duration of the data logging, due to limited memory. The machines are operated in no-load condition with closed-loop speed and current control. Flux-producing current references are set to 2.23A (corresponding to approximately 75% of the actual rated flux, due to the dc-bus voltage limitation) and the dead time is set to 3μs. Relevant parameters and other data are given in Table II.

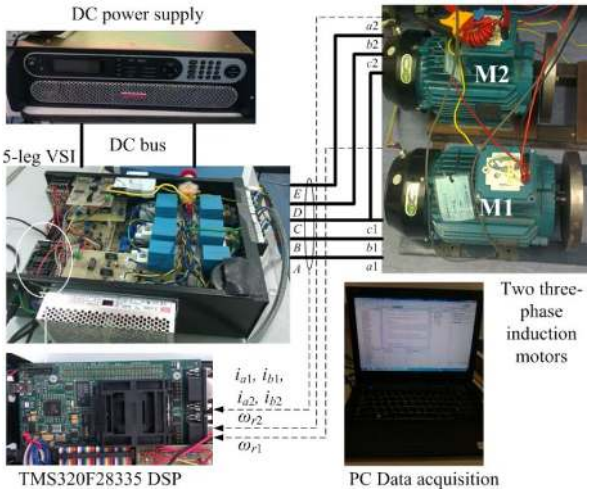

Fig. 6. Experimental test rig.

The highest combination of motor speeds is assumed to be 50π rad/s, i.e. the synchronous electrical speed of an individual machine. Fig. 7 shows the stator *d*- and *q*-axis currents of both machines for all control schemes at the speeds of 40π rad/s for Machine-1 (M1) and 10π rad/s for Machine-2 (M2). Phase-*a* currents of both machines and the common inverter leg-*C* current are shown together. The leg-*C* current is the sum of the two phase-*c* currents of the two machines. All FCS-MPC schemes are capable of tracking the given flux and torque producing current references, leading to proper speed tracking of both machines. Nevertheless, it can be noticed that the current quality is different among the control schemes. Ripples in the machine currents do not participate in the average electromagnetic torque development but cause higher joule losses. Thus, a more comprehensive analysis of the current quality and the average switching frequency is given in what follows.

For all schemes including the PI-PWM control, Machine-1 is subjected to the motor speed references from 5π to 40π rad/s, at steps of 5π rad/s, while Machine-2 remains always at 10π rad/s. Since the machines are not loaded, the slip speeds in steady-state are negligible. Thus these settings result in stator fundamental frequencies of 5 to 40Hz for Machine-1 and 10Hz for Machine-2. Since the FCS-MPC is a non-constant switching frequency control method, the ripple content (or total harmonic distortion) of each phase current will not be the same. The current control quality is thus analyzed based on the average of the phase current ripple content, which is calculated from the synchronous current components. The average current ripple is

$$\frac{1}{\sqrt{2}}\sqrt{[RMS(i_{sd}-mean(i_{sd}))]^2+[RMS(i_{sq}-mean(i_{sq}))]^2} \quad (16)$$

In addition, the average switching frequency is also computed, using

$$(1/2n)\,(\text{Total number of commutations per second}) \quad (17)$$

Evaluation of (16) uses the steady-state stator *d*- and *q*-axis currents. Their mean values are in essence the fundamental components in the phase currents and are removed to obtain the averaged ripple content. Calculation in (17) is based on the commutation count over 1s interval and this duration always corresponds to integer multiples of the fundamental periods for every considered operating

TABLE II
PARAMETERS OF THE INDUCTION MACHINES AND THE EXPERIMENTAL CONDITIONS

Parameter	Value	
FCS-MPC sampling frequency	16 kHz	
PWM switching frequency	3.2 kHz	
DC-bus voltage	450 V	
	Machine-1	Machine-2
Stator phase resistance	2.43 Ω	2.43 Ω
Stator leakage inductance	11.9 mH	12.3 mH
Mutual inductance	296 mH	308 mH
Rotor phase resistance	2.3 Ω	2.3 Ω
Rotor leakage inductance	11.9 mH	12.3 mH
Rated frequency	50 Hz	
Pole pairs	2	

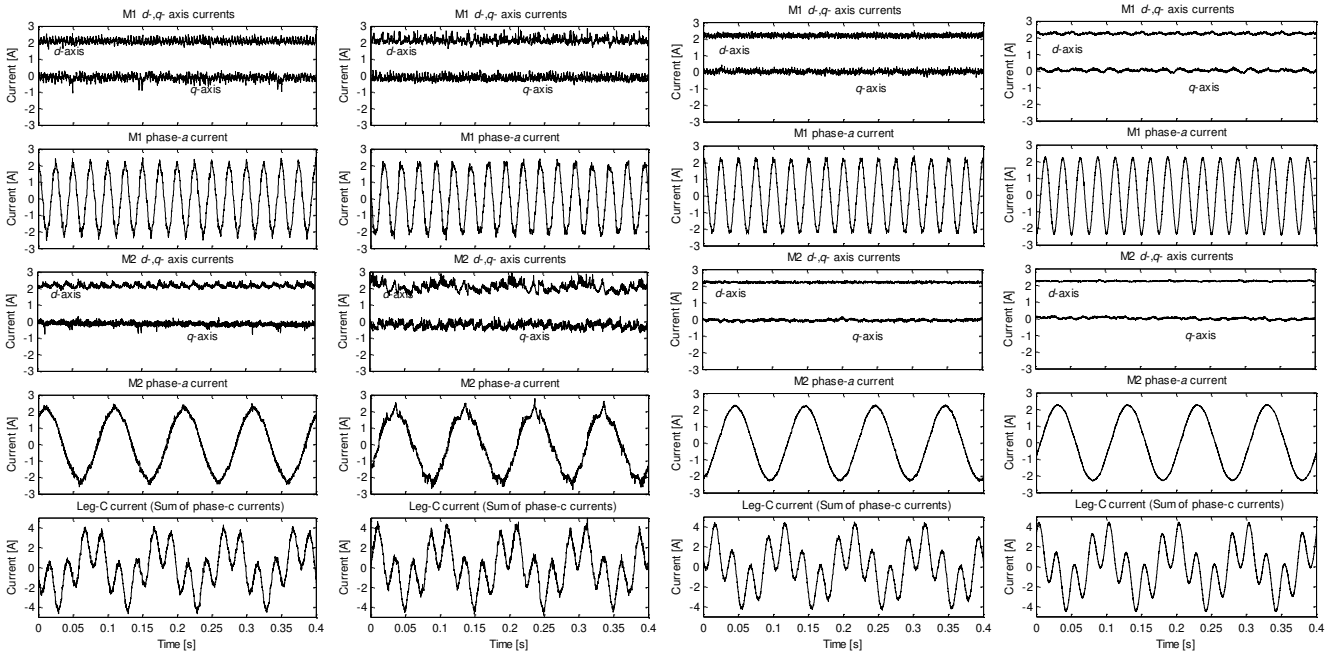

(a) (b) (c) (d)

Fig. 7. Stator *d*- and *q*- axis currents and phase-*a* currents of Machine-1(M1) and Machine-2(M2) at 40Hz and 10Hz stator fundamental frequencies. The common leg-*C* is also shown. (a) MPC1, (b) MPC2, (c) MPC3, (d) PI-PWM control.

point. The five current ripple values for different fundamental frequencies in Fig. 8 (to be discussed next) have been obtained using (16) over the first five consecutive fundamental periods of the waveform within the same 1s overall measurement duration, used for evaluation of (17). The switching frequency data points in Fig. 9 (again five per operating condition, but these are not shown individually in Fig. 9 – instead, fitted curve is given) have been obtained from the same 1s interval measurements, but using five consecutive sub-intervals of 0.2s duration, which also always corresponds to integer multiples of the fundamental periods.

Fig. 8 shows the summary of the average current ripples with respect to Machine-1 fundamental frequency. Note that, due to the control nature, the magnitude of the current ripple does not remain constant from one fundamental period to the other, but varies slightly, so that more data points appear at each frequency. Therefore, a least-square curve fitting method based on the second order polynomial has been adopted to obtain the profile representing the current ripple variation with the machine's operating frequency. MPC2 shows the highest values of the current ripple. This is because sub-optimality is inherently present in the MPC2 due to the *a priori* restriction of actual voltage vectors. MPC1 shows a much better current ripple performance, since all possible voltage vectors per machine are included, i.e. the full set of 32 five-leg VSI switching states is considered. MPC2 exhibits notable low frequency harmonics (Fig. 7b) in the *d*- and *q*-axis currents of M2, which are not present in other schemes. These are undesirable, as they could lead to mechanical load resonances. MPC3 produces the best current ripple performance among the predictive schemes in all operating points. Although it is possible in this case to improve the MPC2 performance by using higher sampling frequency, it is however not feasible for cases with more machines as the computational burden of MPC2 (and MPC1) increases exponentially with the number of machines (and becomes critical for cases demanding very high sampling frequency). Therefore, with regard to the current quality and implementation considerations, MPC3 is a better choice than the other options.

Fig. 9 summarizes the average switching frequency profiles (using the same curve fitting method and averaged values from five separate 0.2s intervals, which differ insignificantly) for the control schemes. The switching frequency of the PI-PWM control scheme is set as 3.2kHz – a value chosen based on the profiles of MPC1 and MPC2. It can be seen that the FCS-MPC schemes result in average switching frequencies that change significantly with the machine operating point, and different schemes essentially occupy different ranges of values. Despite having the lowest average switching frequency range, MPC2 is inferior due to the high current ripples, compared to the MPC1 and MPC3. On the other hand, the MPC3 achieves better current ripple performance at the expense of high average switching frequency. The MPC1 occupies the middle ranges of current ripples and average switching frequencies.

Figs. 7-9 also show that the PI-PWM control gives the best steady-state performance in terms of current ripples and switching losses. This is explained by the use of voltage modulator which is capable of shifting the main voltage switching harmonics into high frequency region (around multiples of the switching frequency), and this leads to lower current harmonics due to the high impedance nature. It should be noted that, despite constant switching frequency in the PI-PWM control, small dispersion of experimentally evaluated values can be seen in Fig. 8 for M1 at frequencies above 10Hz. This is assigned to the fact that the evaluation is done over one fundamental cycle of the M1; since M2 always runs at 10Hz, this means that M1 ripple evaluation is done at different portions of the M2 current, so that the dead-time induced voltage errors are different. All the considered FCS-MPC schemes yield worse performance, since, as shown in Fig. 10, a significant portion of the switching harmonics is found in the low frequency region.

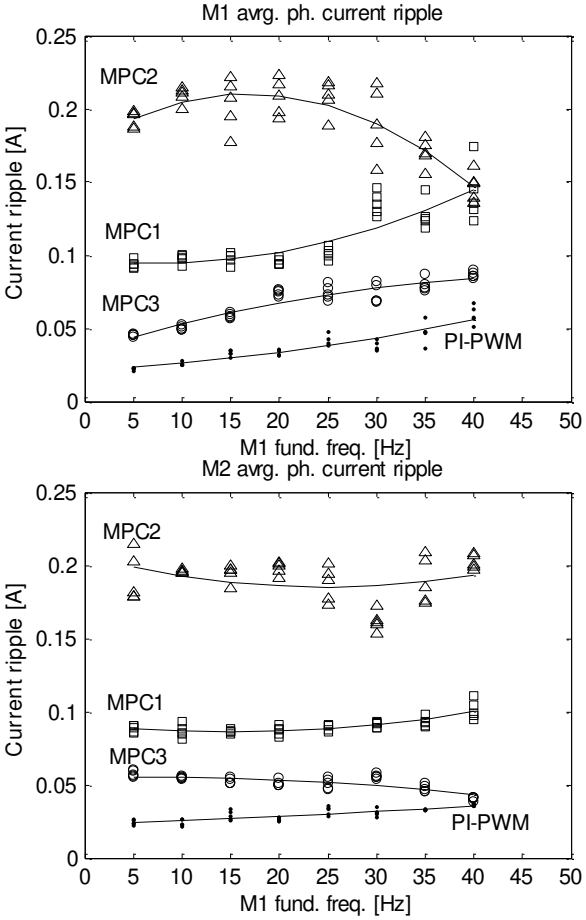

Fig. 8. Variation of the average current ripples of Machine-1 (M1) and Machine-2 (M2) with respect to M1 stator fundamental frequency. Legend is the same as in Fig. 9.

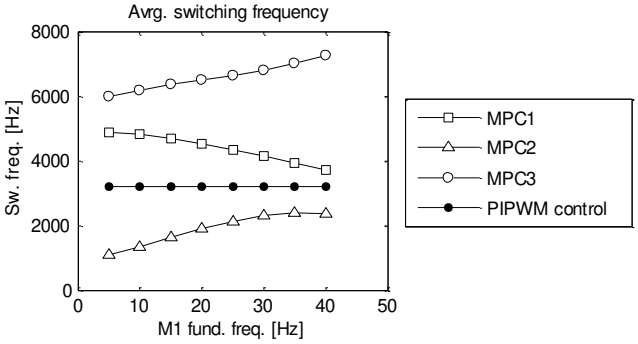

Fig. 9. Variation of the average switching frequency of the five-leg inverter with respect to M1 stator fundamental frequency for the FCS-MPC and the PI-PWM control schemes.

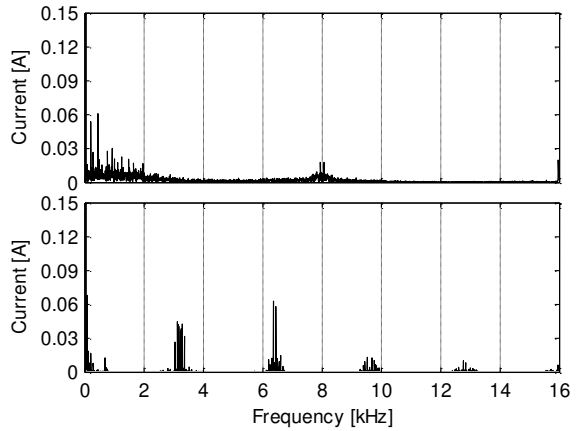

Fig. 10. Machine-1 phase-*a* current's FFT showing the distribution of current harmonics for MPC3 (top) and PI-PWM control (bottom). Operating point as in Fig. 7.

V. Transient Performance Comparison

Fig. 11 shows the comparison of the considered control schemes when M1 is subjected to speed step from 0 to 35π rad/s, while M2 runs at 10π rad/s. The control schemes have practically the same speed response. Fig. 12 shows zoomed extracts of the test depicted in Fig. 11, so that electrical transients can be appreciated better (time interval is from 0.199s to 0.205s, i.e. about 96 sampling instants). It can be seen that the MPC1 and MPC2 develop the fastest current, and hence also torque transients. This agrees with the theoretical expectations as MPC1 and MPC2 use only active vectors throughout the torque current build-up interval (0.2s to 0.201s), shown in Fig. 12. There is a very slight disturbance on the other machine in the case of MPC1 (and even smaller one for the MPC2), caused by the use of single cost function for simultaneous tracking of four current components. On the other hand, MPC3 shows slightly slower torque current build-up; this is understandable as only half of the dc voltage reserve is used for the current of the first machine, as explained in Section III-C. As expected, a complete decoupling between the two machines is realized, due to the use of two separately optimized cost functions. Evolution of the duty ratios in MPC3 with respect to the machine operating points in Fig. 11 is shown in Fig. 13. Transient given by the PI-PWM control is nearly as fast as MPC3 but has a long settling time, prolonged *q*-axis current overshoot, and a slight disturbance in the *d*-axis current. It should be emphasized that the performance of PI-PWM control depends heavily on the parameters of the PI current controllers, and the best possible results have been shown here.

VI. Discussion

When switching loss is taken into account, all three FCS-MPC schemes seem to have very similar performance and it becomes difficult to identify the best scheme. However, for the same sampling frequency, MPC3 gives the best current quality while ensuring a perfect decoupling between the machines even during large transient. Moreover, it eliminates the exponentially-increasing computational complexity with the number of inverter legs, and hence in general imposes the lowest computational burden, compared to MPC1 and MPC2. The worst current quality is obtained with the MPC2, which has the lowest average switching frequency. This implies that minimizing the control input set by considering the neighboring voltage vectors only, as done in the initial study in [9], should be avoided in the considered drive configuration. Application of the PI-PWM gives the lowest steady-state current ripple. This is achieved even with much lower switching frequency than the average switching frequencies of MPC1 and MPC3 are. The explanation is that the PWM shifts the voltage switching harmonics to the high frequency range. In contrast, all FCS-MPC schemes with fixed-width pulses (including MPC3 in a small time scale) produce significant amount of low frequency current harmonics (Fig. 10).

All control schemes give practically the same speed response. With regard to the electrical transient, MPC1 and MPC2 are the fastest. MPC3 is slightly slower, but it guarantees excellent decoupling between the machines. PI-PWM is slower and it has a prolonged overshoot.

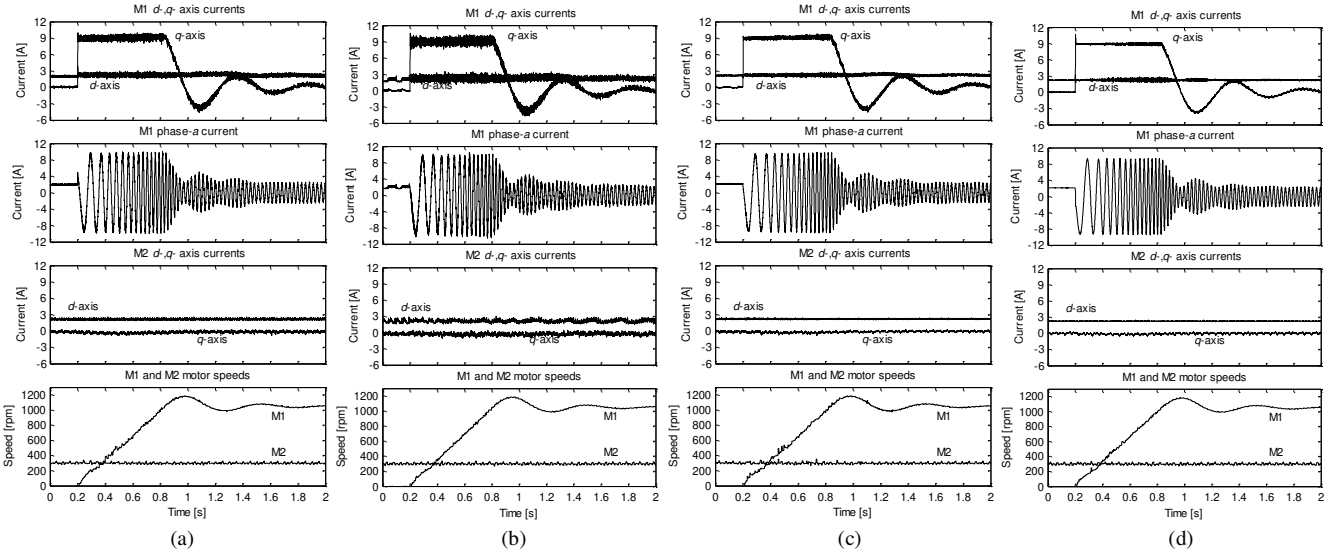

Fig. 11. M1 is subjected to a speed step from 0 to 35π rad/s at 0.2s while M2 runs at 10π rad/s at all times. Stator *d*- and *q*- axis currents and phase-*a* currents of Machine-1(M1) and stator *d*- and *q*- axis currents of Machine-2(M2) are shown. (a) MPC1, (b) MPC2, (c) MPC3, (d) PI-PWM control.

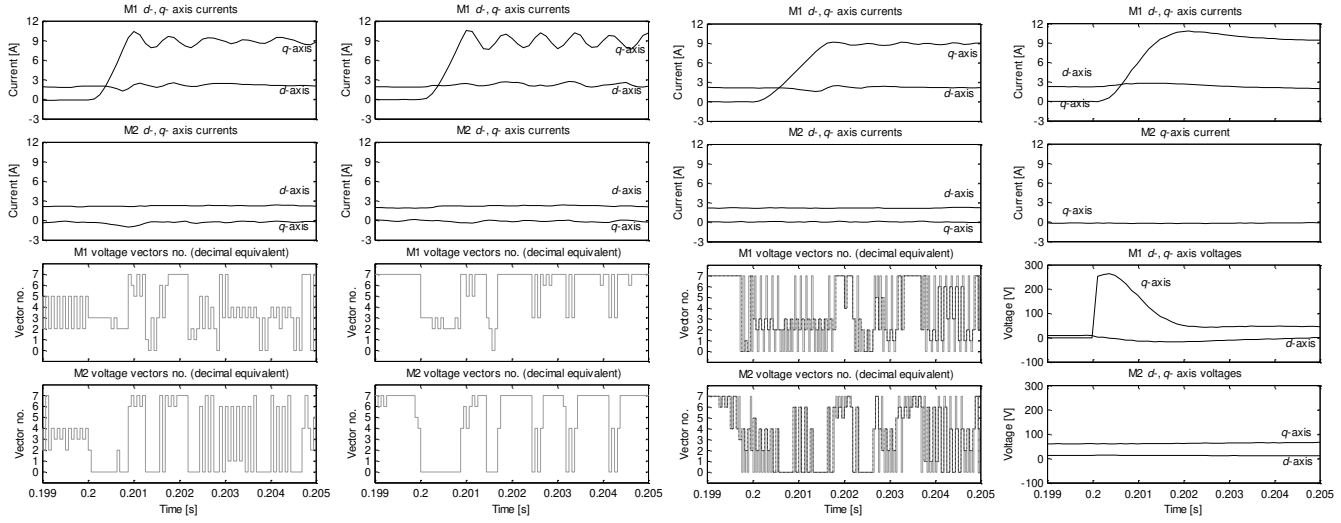

Fig. 12. Close view of the current transient during speed stepping of M1 in Fig. 11. Transitions of voltage vectors expressed in the decimal equivalent of the corresponding switching states are shown for the FCS-MPC schemes. (a) MPC1, (b) MPC2, (c) MPC3 (black lines represent the chosen vectors; grey traces represent the actual sequence of vectors being applied, obtained through post processing using the duty ratios), (d) PI-PWM. Stator *d*- and *q*- axis voltages for the PI-PWM control are shown (i_{sd2} is omitted due to the limited number of data logging channels).

Parameter uncertainty is another important issue in the model based current control schemes. All the predictive schemes studied here, as well as the conventional PI-PWM control scheme, use the same indirect principle in estimating the rotor flux position. Hence, the parameter dependence properties of the rotor flux oriented control apply to a large extent here as well. This has been confirmed in [10] with regard to the rotor resistance detuning, where the FCS-MPC scheme used the same method of rotor flux position estimation as in this study.

VII. Conclusion

Control algorithms for three FCS-MPC schemes have been presented, together with the field-oriented control with PI current controllers and PWM, for a two-motor three-phase drive supplied form a five-leg inverter. The performance has been analyzed in detail using experimentally recorded data. It is noted that all the control schemes have been designed/tuned to give the best possible performance through careful consideration of switching commutations and proper tuning of the PI speed and current controllers.

In terms of steady-state performance, PI-PWM control gives the best performance. On the other hand, all FCS-MPC schemes have faster torque transient than the PI-PWM control. The tuning of FCS-MPC scheme is practically effortless, in contrast to that of PI-PWM control. It is concluded that two control methods have different advantages and the selection of the control method depends on which advantage matters the most.

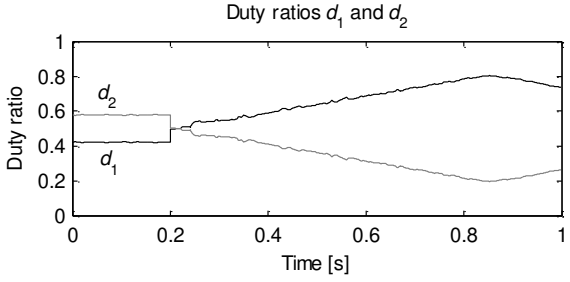

Fig. 13. Evolution of duty ratios d_1 and d_2 of MPC3 for operation in Fig. 11.

Finally, it appears that the best outcome can be produced by combining PWM with model predictive control. Such control method is expected to have advantages of fast transient, effortless tuning and excellent steady-state current ripple. This principle in essence aligns with the one given by the continuous-control-set model predictive control, which has received significantly less attention than the finite-control-set counterpart until now. Hence, this is an area where the future work should be directed to.

Appendix

To consider all the five-leg inverter switching states in MPC, let **S**1 and **S**2 be the three-phase switching states of M1 and M2. The following algorithm is adopted:

START:
$J_{\min} = \infty$;
for each **S**1
  for each **S**2
    if $(|s_{c,1} - s_{c,2}| = 0)$ (18)
      $J = j_{M1} + \lambda_i j_{M2}$
      if $(J < J_{\min})$
        $J_{\min} = J$;
        $\mathbf{S}1_{\min} = \mathbf{S}1$;
        $\mathbf{S}2_{\min} = \mathbf{S}2$;
      end
    end
  end
end
END.

Here $s_{c,1}$ and $s_{c,2}$ are the phase-*c* states of **S**1 and **S**2. An alternative to this algorithm is to replace J in (18) with $j_{M1}+\lambda_i\, j_{M2}+\lambda_{leg}|\, s_{c,1}\text{-}s_{c,2}|$, where λ_{leg} is a high-value weighting factor that penalizes the difference between phase-*c* states, and to also remove the immediate if-else statement containing J. But this method would incur higher computational cost, since cost values for non-feasible combinations of **S**1 and **S**2 would have to be computed as well.

References

[1] D. Dujic, M. Jones, S. N. Vukosavic, and E. Levi, "A general PWM method for a (2n+1)-leg inverter supplying n three-phase machines,"

IEEE Trans. on Industrial Electronics, vol. 56, no. 10, pp. 4107-4118, 2009.

[2] J. Rodriguez, J. Pontt, C. Silva, P. Correa, P. Lezana, P. Cortés, and U. Ammann, "Predictive current control of a voltage source inverter," *IEEE Trans. on Industrial Electronics*, vol. 54, no. 1, pp. 495-503, 2007.

[3] J. Rodriguez, R. M. Kennel, J. R. Espinoza, M. Trincado, C. A. Silva, and C. A. Rojas, "High-performance control strategies for electrical drives: an experimental assessment," *IEEE Trans. on Industrial Electronics*, vol. 59, no. 2, pp. 812-820, 2012.

[4] J. Riveros, F. Barrero, E. Levi, M. Duran, S. Toral, and M. Jones, "Variable speed five-phase induction motor drive based on predictive torque control," *IEEE Trans. on Industrial Electronics*, vol. 60, no. 8, pp. 2957-2968, 2013.

[5] M. Preindl and S. Bolognani, "Model predictive direct speed control with finite control set of PMSM drive systems," *IEEE Trans. on Power Electronics*, vol. 28, no. 2, pp. 1007-1015, 2013.

[6] P. Alkorta, O. Barambones, J. Cortajarena, A. Zubizarrreta, "Efficient multivariable generalized predictive control for sensorless induction motor drives," *IEEE Trans. on Industrial Electronics*, 2014 (d.o.i. 10.1109/TIE.2013.2281172).

[7] P. Cortés, A. Wilson, J. Rodriguez, S. Kouro, and H. Abu-Rub, "Model predictive control of multilevel cascaded H-bridge inverters," *IEEE Trans. on Industrial Electronics*, vol. 57, no. 8, pp. 2691-2699, 2010.

[8] M. J. Duran, J. Prieto, F. Barrero, and S. Toral, "Predictive current control of dual three-phase drives using restrained search techniques," *IEEE Trans. on Industrial Electronics*, vol. 58, no. 8, pp. 3253-3263, 2011.

[9] C. S. Lim, N. A. Rahim, W. P. Hew, and E. Levi, "Model predictive control of a two-motor drive with five-leg inverter supply," *IEEE Trans. on Industrial Electronics*, vol. 60, no. 1, pp. 54-65, 2013.

[10] C. S. Lim, E. Levi, M. Jones, N. A. Rahim, and W. P. Hew, "FCS-MPC based current control of a five-phase induction motor and its comparison with PI-PWM control," *IEEE Trans. on Industrial Electronics*, vol. vol. 61, no. 1, pp. 149-163, 2014.

[11] M. Jones, S. N. Vukosavic, D. Dujic, E. Levi, and P. Wright, "Five-leg inverter PWM technique for reduced switch count two-motor constant power applications," *IET Electric Power Applications*, vol. 2, no. 5, pp. 275-287, 2008.

[12] S. Bolognani, L. Peretti, and M. Zigliotto, "Design and Implementation of model predictive control for electrical motor drives," *IEEE Trans. on Industrial Electronics*, vol. 56, no. 6, pp. 1925-1936, 2009.

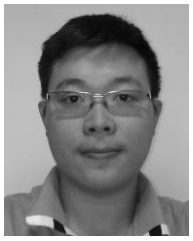

Chee-Shen Lim (S'10) received the BEng degree (Hons.) in Electrical Engineering from the University of Malaya, Malaysia in 2009. He studied on a joint PhD degree programme at the University of Malaya and Liverpool John Moores University, Liverpool, UK from 2010 until July 2013, when he was awarded his PhD. He is with the Power Energy Dedicated Advanced Center (UMPEDAC), University of Malaya, Kuala Lumpur. His research interests include high performance drives and embedded real-time control.

Emil Levi (S'89, M'92, SM'99, F'09) received his M.Sc. and PhD degrees from the University of Belgrade, Yugoslavia in 1986 and 1990, respectively. From 1982 till 1992 he was with the Dept. of Elec. Engineering, University of Novi Sad. He joined Liverpool John Moores University, UK in May 1992 and is since September 2000 Professor of Electric Machines and Drives. He serves as Co-Editor-in-Chief of the IEEE Trans. on Industrial Electronics, as an Editor of the IEEE Trans. on Energy Conversion, and as Editor-in-Chief of the IET Electric Power Applications. Emil is the recipient of the Cyril Veinott award of the IEEE Power and Energy Society for 2009.

Martin Jones received his BEng degree (First Class Honours) in Electrical Engineering from the Liverpool John Moores University, UK in 2001. He was a research student at the Liverpool John Moores University from September 2001 till Spring 2005, when he received his PhD degree. Dr Jones was a recipient of the IEE Robinson Research Scholarship for his PhD studies and is currently with Liverpool John Moores University as a Reader. His research is in the area of high performance ac drives.

Nasrudin A. Rahim (M'89, SM'08) received the B.Sc. (Hons.) and M.Sc. degrees from the University of Strathclyde, Glasgow, U.K., and the PhD degree from Heriot–Watt University, Edinburgh, U.K., in 1995. He is currently a Professor with the Faculty of Engineering, University of Malaya, Kuala Lumpur, Malaysia, where he is also the Director of the Power Energy Dedicated Advanced Center (UMPEDAC). Prof. Rahim is a Fellow of the IET, U.K., and the Academy of Sciences Malaysia.

Wooi-Ping Hew (M'06) obtained his BEng and Masters (Electrical) degrees from the University of Technology, Malaysia. He received his PhD from the University of Malaya, Kuala Lumpur, Malaysia in 2000. He is currently a Professor in the Faculty of Engineering, University of Malaya, Kuala Lumpur, Malaysia. Dr. Hew is a Member of IET and a Chartered Engineer. His research interests include electrical drives and electrical machine design.